

# Upscaling Effects on Alkali Metal-Grafted Ultrastable Y Zeolite Extrudates for Modeled Catalytic Deoxygenation of Bio-oils

Ana M. Hernández-Giménez,<sup>[a]</sup> Laura M. de Kort,<sup>[a]</sup> Gareth T. Whiting,<sup>[a]</sup> Héctor Hernando,<sup>[b]</sup> Begoña Puértolas,<sup>[c]</sup> Javier Pérez-Ramírez,<sup>[c]</sup> David P. Serrano,<sup>[b, d]</sup> Pieter C. A. Bruijninx,<sup>[a, e]</sup> and Bert M. Weckhuysen<sup>\*[a]</sup>

Developing efficient solid catalysts is necessary when for example moving from batch chemistry to continuous flow systems. In this work, scale-up effects of zeolite-based catalyst materials have been tested in aldol condensation as a model reaction for bio-oil upgrading via deoxygenation. For this purpose, shaped catalyst bodies were obtained via extrusion of ultrastable Y zeolite (USY) using either attapulgite (Att.) or bentonite (Bent.) as clay binder, followed by post-alkali metal ion grafting of K<sup>+</sup> after (rather than before) extrusion. This approach proved essential to preserve the catalysts' crystallinity. The Att.-bound catalyst body was more active than its Bent.-counterpart, correlating well with the observed changes in physicochemical properties. The K-(USY/Att.) catalyst showed

new basic oxygen and strong Lewis acidic sites resulting from clay incorporation, in addition to the Lewis acid (K<sup>+</sup>) and basic sites (K–OH) created upon grafting. For K-(USY/Bent.), the grafting proved less efficient, likely due to pore blockage caused by the binder. Bent. addition resulted in acid sites of moderate Brønsted and strong Lewis acidity, but hardly any of the basicity desired for the aldol condensation reaction. The poor potassium grafting yet led to some cation exchange with the binder (likely with the Na<sup>+</sup> naturally present in the Bent. material). The results obtained demonstrate the critical importance of the choice of the binder material and the synthesis protocol adopted for upscaling solid base materials in the form of catalyst bodies.

## 1. Introduction

The bio-oils that are typically obtained from lignocellulosic biomass, e.g. by (catalytic) fast pyrolysis, require extensive upgrading to improve their quality by reducing their oxygen content and increasing the average carbon chain length. Given the high content of aldehydes in bio-oil,<sup>[1]</sup> both goals can be achieved by aldol condensation and hence this has been proposed as an intermediate stage deoxygenation step for pyrolysis oil upgrading to advanced second-generation bio-fuels.<sup>[2]</sup> Aldol condensation is typically catalyzed by acid-base pairs<sup>[3–4]</sup> or by solid bases.<sup>[5]</sup> Catalysts with mild base strength, such as hydroxyapatites<sup>[6]</sup> and alkali metal-grafted zeolites,<sup>[7–9]</sup> have shown to perform very well in this reaction. The methodology for depositing non-noble metals into zeolite-based catalysts by means of ion-exchange (i.e., immersion of the catalyst into a metal solution bath) is well-known and applied in industry for many years.<sup>[10]</sup> In such methodology, for example, special attention has been paid to metal concentration and the solution bath pH.<sup>[10]</sup>

The resulting mildly basic alkali grafted-materials consist of ultrastable Y zeolite (i.e., USY) with high Si/Al ratios of ~400, obtained via dealumination.<sup>[11]</sup> The silanol groups located at defect sites in these materials are easily deprotonated, so that metalation readily occurs in alcoholic solutions of alkali metal hydroxides, forming the basic sites.<sup>[8]</sup> The grafted alkali ions, which are coordinated to at least two oxygen atoms, stabilize the local environment<sup>[12]</sup> and are considered responsible for the excellent catalytic performance of these materials. From the

[a] A. M. Hernández-Giménez, L. M. de Kort, G. T. Whiting, P. C. A. Bruijninx, B. M. Weckhuysen  
Inorganic Chemistry and Catalysis, Debye Institute for Nanomaterials Science


Utrecht University  
Universiteitsweg 99  
3584 CG Utrecht (The Netherlands)  
E-mail: B.M.Weckhuysen@uu.nl


[b] H. Hernando, D. P. Serrano  
Thermochemical Processes Unit  
IMDEA Energy Institute  
28935, Móstoles, Madrid (Spain)

[c] B. Puértolas, J. Pérez-Ramírez  
Institute for Chemical and Bioengineering  
Department of Chemistry and Applied Biosciences  
ETH Zurich  
Vladimir-Prelog-Weg 1  
8093, Zurich (Switzerland)

[d] D. P. Serrano  
Environmental and Chemical Engineering Group  
Rey Juan Carlos University  
28933, Móstoles, Madrid (Spain)

[e] P. C. A. Bruijninx  
Organic Chemistry and Catalysis  
Debye Institute for Nanomaterials Science  
Utrecht University  
Universiteitsweg 99  
3584 CG Utrecht (The Netherlands)

 Supporting information for this article is available on the WWW under <https://doi.org/10.1002/cctc.202001840>

 © 2021 The Authors. ChemCatChem published by Wiley-VCH GmbH. This is an open access article under the terms of the Creative Commons Attribution License, which permits use, distribution and reproduction in any medium, provided the original work is properly cited.

different alkaline metals and synthesis conditions tested, treatment of zeolite USY with 0.1 M KOH in methanol led to the most active and stable catalytic material for the vapor-phase aldol condensation of propanal (which was selected as model reaction for bio-oil upgrading).<sup>[8–9]</sup> Keller *et al.* reported excellent activities, as well as stability with increasing time-on-stream and selectivities of 90% towards the desired pathway, with only limited activity towards the competitive Tishchenko reaction,<sup>[13]</sup> which is favored by stronger bases. Likewise, this catalytic system has been coupled in series with a zeolite ZSM-5-based catalyst, showing its high activity for aldol condensation and ketonization reactions, as well as for the conversion of oligomers in bio-oil, thus producing liquid organic fractions with low oxygen content.<sup>[14]</sup> These promising results encouraged the study of shaped K-grafted USY catalysts to evaluate the scalability of this technology for potential use in industrial-scale reactors.

Upscaling of a catalytic bio-oil upgrading process from lab-scale to pilot-plant scale requires adaptation of the powdered catalysts to shaped ones for practical handling and application in larger chemical reactors.<sup>[15–16]</sup> Catalysts in their technical form are often millimeter-sized bodies that are composed of multiple, carefully selected components, in addition to the primary active phase, e.g., the zeolite, to improve transport, mechanical strength and chemical stability and should ideally perform as well as their powdered parent material (on an active phase weight-to-weight basis).<sup>[17]</sup> However, the size and shape of technical catalysts influence the catalytic activity, internal and external mass transport, mechanical particle resistance and pressure drop in large scale reactors.<sup>[18]</sup> These technical catalyst bodies can be prepared by several methods, e.g., pelletization, granulation and extrusion,<sup>[19]</sup> with the latter being the most economic and most commonly applied.

In addition to the shape of the technical catalyst material, the selection of the binder material, as well as the proportions used, is of crucial importance.<sup>[20]</sup> It will influence the catalytic performance by the manner and extent to which the porosity, morphology and chemical composition, e.g., by ion exchange, are modified.<sup>[21]</sup> For zeolite-based materials, which have poor self-binding properties, the inclusion of binders is essential for attaining durable bodies<sup>[16]</sup> with the required strength and attrition resistance for operating upon continuous mode at industrial utilities. Typically, alumina, silica or clays are used as binder materials for shaping zeolites.<sup>[22–23]</sup> Recently, Verkleij *et al.* reported evidences on how the selection of alumina or silica as binder for a ZSM-5 zeolite-based catalyst extrudate can truncate a given reaction selectivity. For instance, in the transalkylation of toluene with 1,2,4-trimethylbenzene (1,2,4-TMB) the incorporation of Al<sub>2</sub>O<sub>3</sub> as binder created new acid sites that promoted isomerization which hindered the product selectivity,<sup>[24–25]</sup> while SiO<sub>2</sub> binder promoted it. Techniques, such as the confocal fluorescence microscopy and UV-Vis diffuse reflectance microspectroscopy, performed under *operando* conditions were used to assess this finding with visual evidence. The contrary was seen in the 1-hexene oligomerization reaction where Al<sub>2</sub>O<sub>3</sub> is preferred as binder rather than SiO<sub>2</sub> to assist the ZSM-5 zeolite activity. In that case, the isomerization activity of Al<sub>2</sub>O<sub>3</sub>, as a

consequence of its type of acidity, is found to promote the elongation of the (isomerized) hexene.<sup>[26]</sup>

Numerous examples of technical zeolite-based catalyst bodies using clays as binder materials are found in literature for a variety of reactions. The mobile alkali and alkaline earth cations present in clays can easily exchange with Brønsted and Lewis acid sites in the zeolite framework, usually with important impact on the catalytic performance.<sup>[21–22]</sup> For example, Uguina *et al.* investigated toluene disproportionation over pelletized ZSM-5 zeolite/montmorillonite extrudates, denoting an important toluene conversion decrease upon agglomeration. Yet, the catalytic activity of the pellets could be restored almost completely (i.e. regarding the activity shown by the parent zeolite) by subsequent HCl ion-exchange and calcination.<sup>[27]</sup> De Lucas *et al.* reported on technical catalysts consisting of bentonite as binder and mordenite, β- or ZSM-5 zeolites as active phase for n-paraffin hydro-isomerization reactions.<sup>[28–30]</sup> In the case of the mordenite and ZSM-5 zeolitic materials, the strong decrease in acidity provoked by the ion exchange between the zeolite and the binder resulted in a decreased conversion, yet with a concomitant selectivity towards branched products enhancement, owing to the meso- and macroporosity provided by the bentonite. As for the β zeolite, the additional incorporation of extra-framework Al (EFAl) species led to an improvement in both n-paraffin conversion and also selectivity towards branched products. In the methanol-to-hydrocarbons (MTH) reaction, the incorporation of attapulgite as binder to a ZSM-5 zeolite significantly decreased the concentration in Brønsted acidity, due to ion exchange with Mg<sup>2+</sup> from the clay.<sup>[31]</sup> Consequently, the extrudate's intrinsic activity was attenuated but the light-olefin selectivity and stability were improved. Less invasive was the inclusion of bentonite or methylcellulose as binders on shaped β- and Y zeolites for cyclization of the lemon-like odor citronellal into menthol-like odor pulegol products in continuous mode.<sup>[32]</sup> Despite certain mass-transfers limitations and altered acid properties the final (sum of isomer) products yield was not severely affected.<sup>[32]</sup>

Not only the binder choice matters, but also the preparation method does when tailoring shaped catalytic systems. Zecevic *et al.* reported improved catalytic performances on hydrocracking reactions for bifunctional Pt–Y zeolite catalysts incorporating the metal phase on the binder (Al<sub>2</sub>O<sub>3</sub> in that case) rather than on the zeolite, being the distance between active phases the key for such improvement.<sup>[33]</sup> More recently, Vajglova *et al.* compared the performances of differently prepared bifunctional Pt–β zeolite catalyst extrudates on n-hexane hydro-isomerization.<sup>[34]</sup> For that application the best system was the one in which the metal was deposited exclusively on the zeolite material, followed by the binder incorporation and the subsequent extrusion, based on the enhanced metal-to-acid site ratio.<sup>[34]</sup> In this work, we explore the extrusion of USY zeolite with attapulgite and bentonite as binder materials and the incorporation of potassium by grafting in an alcoholic medium. The impact of the synthesis protocol has been evaluated, i.e., pre- vs. post-grafting on the physicochemical properties of the USY-clay catalyst body.

## 2. Results and Discussion

### 2.1. Catalyst Characterization

#### 2.1.1. Structural and textural properties of catalyst materials

The effect of the addition of binder material (i.e., attapulgite and bentonite, further denoted as respectively Att. and Bent.) on the structural integrity of the zeolite component (i.e., ultrastable Y zeolite, further denoted as USY), i.e., the crystallinity and porosity, were studied by XRD (Figure 1a,b), N<sub>2</sub> (Figure S1) and Ar physisorption (Figure S2, Table 1), respectively. The XRD patterns of both post-grafted technical catalysts are very close to the cubic pattern of zeolite USY (*Fd3-m*),<sup>[35]</sup> PDF 00-045-0112), with additional new features originating from the clay component present. For the K-(USY/Att.) material a new diffraction line emerged at  $\sim 31.1$  ( $2\theta$ )°, attributed to quartz, a common impurity in attapulgite (Figure 1a). The XRD results highlight the importance of performing the K-grafting on the technical catalyst material after extrusion and calcination rather than before. Indeed, the sample grafted prior to shaping

with attapulgite ((K-USY)/Att. Figure 1a), completely lost its crystallinity after extrusion and subsequent calcination. This amorphization process is also reflected in the deterioration of the textural properties of the material, as illustrated in Figure S1.

Exposure to the basic solution in which the grafting is performed already leads to some unavoidable loss in crystallinity. See for example, the XRD pattern of K-USY (red series), which is considerably less intense than the pure zeolite USY (black series). The subsequent exposure to water during the extrusion process may then be responsible for the structural collapse of the catalyst. Grafting of potassium post-extrusion rather than pre-extrusion would then better preserve the catalyst crystallinity, provided that the pH of the solution during grafting is carefully controlled. A downside of the need to resort to the post-grafting method, though, is that with the binder material already present the potassium can also graft to/exchange at other phases of the material than exclusively at the zeolite, thereby introducing other/new sites, which may deteriorate the catalyst performance. The XRD pattern of the K-(USY/Bent.) material, also showed no sign of amorphization, with the

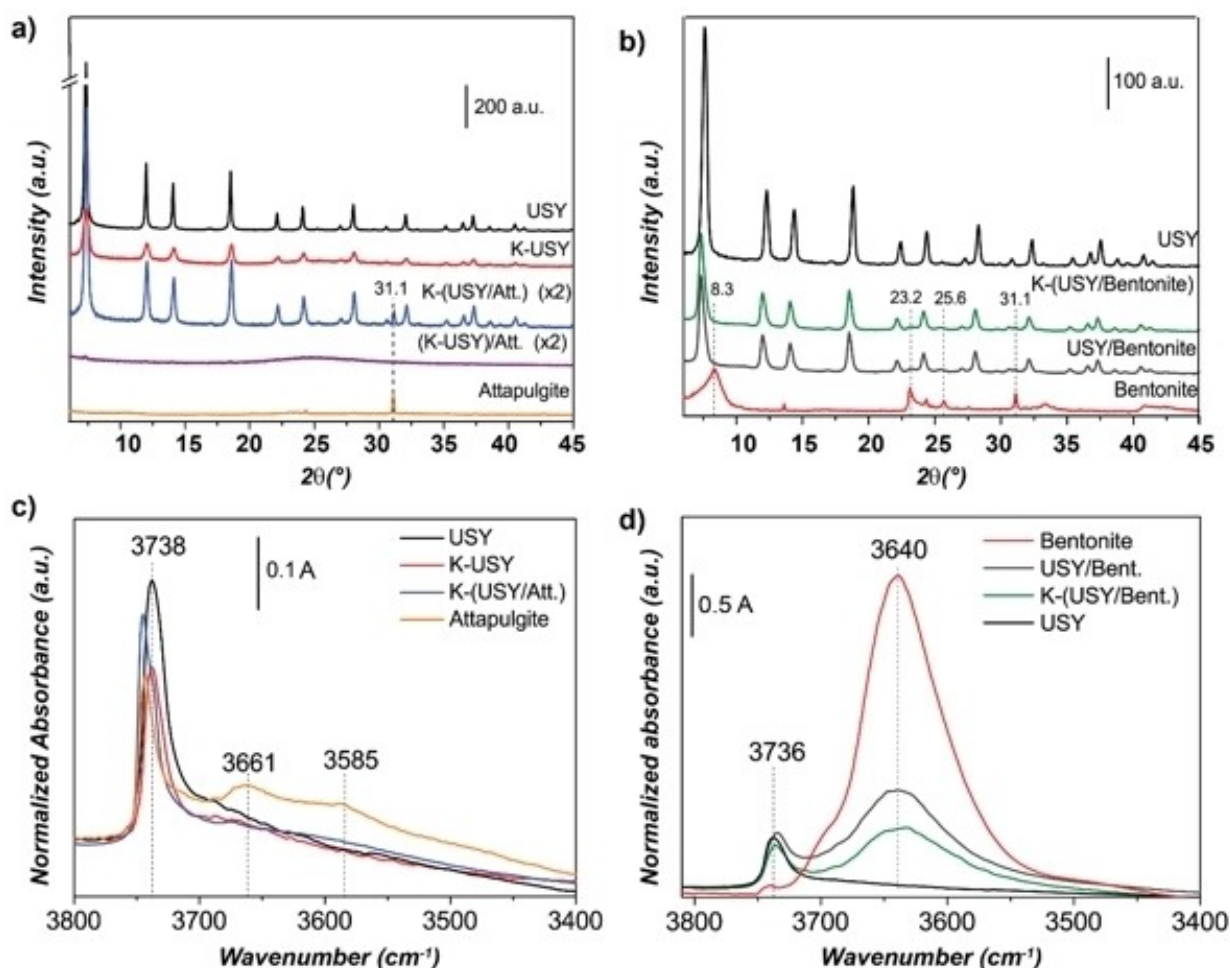


**Figure 1.** (a–b) XRD patterns of the attapulgite-bound (a) and bentonite-bound (b) materials in the range  $2\theta = 6\text{--}45^\circ$ . Note the amorphous nature of the pre-grafted (K-USY)/Att. extrudate (purple line in a). (c–d) Normalized FT-IR spectra of the activated attapulgite-bound (c) and bentonite-bound (d) catalysts series in the region between 3800 and 3400  $\text{cm}^{-1}$ .

**Table 1.** Overview of properties of the catalysts under study, including the two clay materials. For the technical catalysts, theoretical values – based on (K) USY:clay mass ratios– are indicated into brackets.

Catalyst	$S_{\text{BET}}^{[a]}$ [m <sup>2</sup> /g]	$S_{\text{micro}}^{[a]}$ [m <sup>2</sup> /g]	$S_{\text{ext}}^{[a]}$ [m <sup>2</sup> /g]	$V_{\text{pore}}^{[a]}$ [cm <sup>3</sup> /g]	$V_{\text{micropore}}^{[a]}$ [cm <sup>3</sup> /g]	Basic sites <sup>[b]</sup> [μmol/g]	(Lewis) Acid sites <sup>[c]</sup> [μmol/g]	Soft coke <sup>[e]</sup> [wt.%]	Hard coke <sup>[e]</sup> [wt.%]
USY	756	639	117	0.16	0.26	34	–	0.3	0.3
K-USY	590	516	70	0.09	0.27	439	20	1.1	2.2
K-(USY/Att.)	472 (431)	388 (362)	84 (66)	0.15 (0.11)	0.18 (0.19)	244 (396)	15 (31)	0.2; 0.2 <sup>[f]</sup>	2.7; 2.7 <sup>[f]</sup>
Attapulgite	60	2	58	0.14	–	294	55	0.6	5.6
USY/Bent.	490 (537)	375 (450)	114 (87)	0.18 (0.13)	0.17 (0.18)	54 (51)	11 (2)	0; 0.2 <sup>[f]</sup>	2.1; 2.1 <sup>[f]</sup>
K-(USY/Bent.)	526 (421)	440 (364)	86 (54)	0.14 (0.08)	0.18 (0.19)	15 (335)	6 (14)	0.1; 0 <sup>[f]</sup>	1.9; 1.3 <sup>[f]</sup>
Bentonite	27	10	16	0.05	0.004	91	8; (BAS <sup>[d]</sup> = 3)	0.3	3.4

[a] Properties derived from Ar physisorption (Figure S2). [b] Determined from CO<sub>2</sub>-TPD. [c] Determined from Pyridine-FT-IR spectroscopy at 150 °C. [d] BAS=Brønsted acid sites (below 1 μmol/g for USY/Bent. and K-(USY/Bent.) catalysts); non-existent for USY, K-USY, Attapulgite nor K-(USY/Att.) catalysts. [e] Determined by TGA. [f] Second value corresponds to measurements on catalyst bodies instead of wafers.

reflections of the zeolites accompanied with a quartz peak as well as some small peaks at 23.2 and 25.6 (2θ)<sup>o</sup>, all from bentonite.

The textural properties of the technical catalysts were determined by Ar physisorption at –196 °C (Figure S2, Table 1). The isotherms show that K-(USY/Att.) (b) and K-(USY/Bent.) (f) preserved to a large extent the characteristics of the parent USY zeolite, i.e., its characteristic type IV isotherm, typical of mesoporous materials,<sup>[36]</sup> accompanied by a steep H3 hysteresis loop<sup>[37]</sup> (Figure S2a,b,e,f). In contrast, pure attapulgite and bentonite (c,d) showed type II isotherms, typically attributed to meso/macroporous materials, accompanied also by a H3 hysteresis loop. Yet, bentonite (d) showed a considerably lower surface area and pore volume than attapulgite, with also a much narrower pore-size distribution (see inset in Figure S2c,d) which may suggest higher diffusivity constraints. Isotherms of USY/Bent. (e) and K-(USY/Bent.) (f) are similar although the pore-size distribution (see insets in Figure S1c,d) showed reduced pore volume after K-grafting. Also, the K-(USY/Bent.) catalyst showed some increment in surface area (Table 1), due to additional porosity/voids created by the grafting method. Experimental textural values obtained for the different catalyst bodies, namely K-(USY/Att.), K-(USY/Bent.) and USY/Bent., confirm the USY:clay mass ratios.

### 2.1.2. Composition, accessibility and morphology

The potassium content of the technical catalysts was 2.48 wt.% by ICP-OES, for K-(USY/Att.) and 0.85 wt.% for K-(USY/Bent.). Given that attapulgite contains 0.58 wt.% of K, and bentonite 0.45 wt.% (Table S1–S2), this means that for the K-(USY/Att.) catalyst 0.17 wt.% of K resulted from clay incorporation, while 2.31 wt.% was incorporated through the K-grafting process. For the K-(USY/Bent.) catalyst, 0.13 wt.% of K was incorporated upon bentonite addition, and only 0.72 wt.% was incorporated in the technical catalyst as a result of the K-grafting step. The differences in K loading may be related to either mass-transfer limitations due pore blockage upon bentonite incorporation, or to differences in hydrophobicity/hydrophilicity between the zeolite USY and the bentonite phases, attributed to their differences in chemical composition.

The grafting of K<sup>+</sup> onto the technical catalyst material was examined by FT-IR spectroscopy of the OH stretching region, as plotted in Figure 1c,d. It is known that K<sup>+</sup> ions are grafted to deprotonated silanol groups when only the USY zeolite is used.<sup>[12]</sup> This is also at least partly the case for the technical catalyst, as confirmed by changes in the intensity of the ν<sub>OH</sub> band of the USY zeolite, centered at ~3738 cm<sup>-1</sup>; in addition to the intensity of the ν<sub>OH</sub> band of attapulgite, located at ~3738, 3661 and 3585 cm<sup>-1</sup> (Figure 1c), which also decreased upon K-grafting. The same was observed for the bentonite-bound catalyst material (Figure 1d), which showed a significant decrease of the 3640 cm<sup>-1</sup> band intensity upon K-grafting. This observation suggests that K<sup>+</sup> ions coordinate to both deprotonated silanol groups present in the USY active phase, as well as surface-OH groups present in the clay.

SEM-EDX confirmed that considerably lower amounts of K<sup>+</sup> ions were deposited on the bentonite-based extrudates (Figure 2). The distribution of K<sup>+</sup> ions over a cross-section of K-(USY/Att.) (Figure 2c) and K-(USY/Bent.) (Figure 2g) catalysts showed a gradient, starting on the edges and progressively decreasing in intensity in a radial direction inwards, suggesting diffusional constraints, with the distribution over K-(USY/Att.) being more homogeneous. Rich-in-potassium areas coincided with rich-in-clay areas, as indicated by the aluminum distribution (Al is mainly present in the clay (Figure 2b,f), given the poor Al content in the USY zeolite (with a Si/Al ratio of ~400)). However, K was also found in areas with little Al, confirming that K locates on both the zeolite and the clay, as concluded from FT-IR spectroscopy. Possible exchange between K<sup>+</sup> ions and other similar cations naturally present in the clay binders should also be considered. In particular for bentonite extrusion, Na<sup>+</sup> is abundantly present in the clay and could have been exchanged, as illustrated by the Na elemental map (Figure 2h), showing the element to be distributed over the whole catalyst body section (i.e. in agglomerates being rich- or poor in clay). The Mg elemental map for the attapulgite-derived catalyst body (Figure 2d) serves as counterexample, showing that magnesium, present in relatively large amounts in attapulgite (Table S1), is mainly located on the clay aggregates.

Figure S3 includes higher magnifications of the SEM and TEM images of K-USY (Figure S3a–c), displaying the cubic morphology of the sample; K-(USY/Att.) (Figure S3d,f), showing

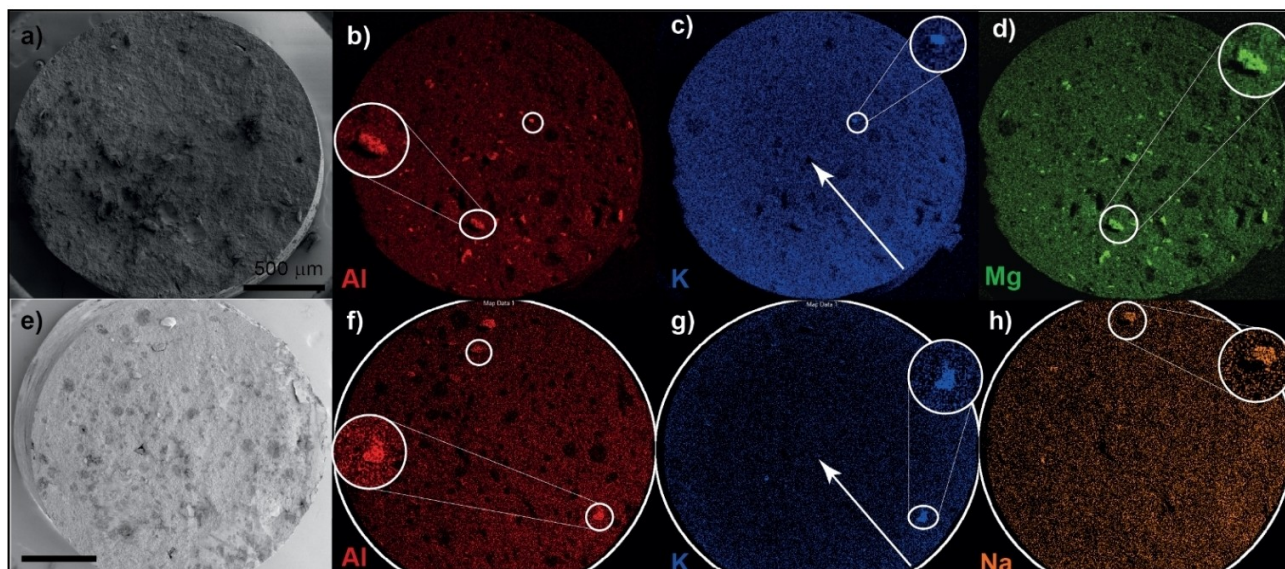


**Figure 2.** (a,e) SEM images of K-(USY/Att.) (a) and K-(USY/Bent.) (e) extrudates. (b–d,c,g–h) EDX maps of Al (red, b,f), K (blue, c,g), Mg (green, d) and Na (orange, h) in the extrudates. Al indicates the clay presence. The same scale (500  $\mu\text{m}$ ) applies for both catalyst bodies. The marked areas correspond to regions containing mainly clay (see them with higher detail in amplified insets); the arrow indicates the K-gradient.

the characteristic needle-like attapulgite,<sup>[38]</sup> (Figure S3e) embracing the cubic zeolite crystals and agglomerating more on crystal edges and defects. K-(USY/Bent.) (Figure S3g,i) shows a homogeneous distribution of USY and bentonite, which has a less defined morphology and mainly consists of non-uniform cubes, flakes, rugged-like and amorphous shapes (Figure S3h).<sup>[39]</sup>

Uptake staining studies of the K-(USY/Att.), K-(USY/Bent.) and USY/Bent. catalyst with fluorescent (polar) microsphere probes of 20 nm size allowed the macro- and mesoscale accessibility of the catalyst bodies to be studied.<sup>[40]</sup> After letting the probe act for 5 min, it was found to diffuse through the entire K-(USY/Att.) extrudate, as shown by the uniformly intense cross-section (Figure 3a,b). However, with the K-(USY/Bent.) catalyst body (Figure 3c,d), the fluorescent beads could only access the edges of the catalyst body ( $\sim 100 \mu\text{m}$ ), with no diffusion seen inwards. Interestingly, the same was seen for the USY/Bent. catalyst body (Figure 3e,f) before grafting, i.e., the fluorescent probe mainly located at the outer edge. This limited accessibility is in line with the low K loading seen for the bentonite catalyst body after grafting. Although the bulk Ar physisorption analysis did not indicate this, the chemical staining studies show that, locally, the bentonite binder material can provoke pore blockage in the catalyst body. Similarly, in the work published by Whiting *et al.* in which bentonite (and kaolinite) clays were used as binders in the MTH reaction over ZSM-5 extrudates, blockage was also observed.<sup>[40]</sup>

### 2.1.3. Basicity and acidity properties

The nature and strength of the basic sites present in the catalyst materials before and after K-grafting and extrusion with the clays were studied by  $\text{CO}_2$ -FT-IR spectroscopy (Figure 4) and

$\text{CO}_2$ -TPD, based on the interaction of the mildly acidic  $\text{CO}_2$  molecule with basic sites. The nature and the distribution of the acid sites in the extrudates were determined by Pyridine-FT-IR spectroscopy (Figure 5).

Figure 4 shows the  $\text{CO}_2$ -FT-IR spectra of the materials, including the pure USY zeolite as reference. For the K-(USY/Att.) catalyst (Figure 4d) multiple bidentate coordinated carbonate species emerged upon interaction of  $\text{CO}_2$  with surface basic sites,<sup>[41–42]</sup> presumably due to oxygen atoms coordinated to the  $\text{K}^+$  species, causing split vibrations at  $\sim 1631$  and  $1371 \text{ cm}^{-1}$ . The splitting of the asymmetric  $\nu_3$  vibration of adsorbed  $\text{CO}_3^{2-}$ ,  $\Delta\nu_3$ , was thus *ca.*  $260 \text{ cm}^{-1}$ , confirming its bidentate coordination mode ( $> 250 \text{ cm}^{-1}$ ).<sup>[41]</sup> These basic sites are present at a larger degree in the K-USY sample (Figure 4b), with stretching bands located at  $1633 \text{ cm}^{-1}$  and  $1349 \text{ cm}^{-1}$  and are again ascribed to a bidentate carbonate coordinated to a  $\text{K}^+$  site, i.e., with a splitting of  $284 \text{ cm}^{-1}$ . The FT-IR bands at  $1682$ – $1668 \text{ cm}^{-1}$  and  $1407 \text{ cm}^{-1}$  correspond to surface bicarbonate species formed by reaction of  $\text{CO}_2$  with OH groups,<sup>[43–45]</sup> indicating also the presence of basic hydroxyl groups (see band arising at  $\sim 3670 \text{ cm}^{-1}$  in inset). In contrast, the absence of any well-defined band in the range of  $\sim 3800$ – $3600 \text{ cm}^{-1}$  for the K-(USY/Att.) catalyst suggests that such hydroxyl groups are not present in the catalyst body.

Both oxygen and hydroxyl basic sites were absent in the USY starting material (Figure 4a) for which upon saturation with  $\text{CO}_2$  dosing solely linearly adsorbed  $\text{CO}_2$  (Figure 4g) at  $\sim 2345 \text{ cm}^{-1}$  (see inset) was observed.<sup>[41]</sup> Attapulgite (Figure 4c), however, showed one bidentate coordinated carbonate species formed at  $\sim 1631$  and  $\sim 1422 \text{ cm}^{-1}$ . The small  $\Delta\nu_3$  splitting of  $\sim 209 \text{ cm}^{-1}$  is indicative of the intermediate strength of its basic sites. Therefore, the K-grafting process generates oxygen and hydroxyl basic sites in the USY zeolite, while the addition of

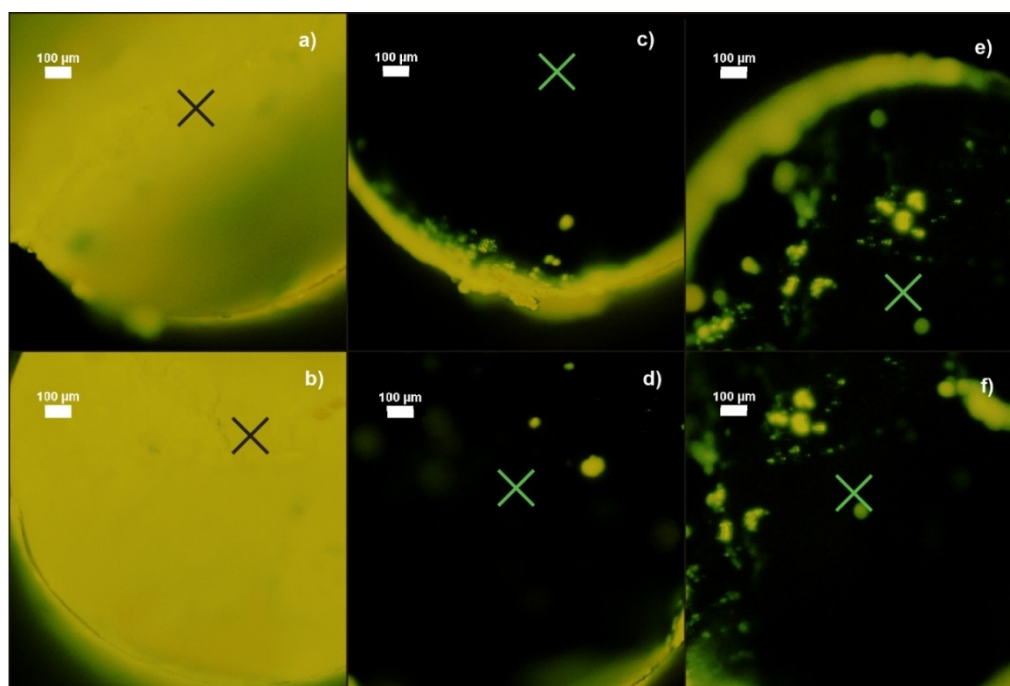


**Figure 3.** Cross-sectioned extrudates chemically stained with yellow FluoSpheres (20 nm), focusing on edges (a,c,e) and centers (b,d,f) of the catalyst bodies as measured with confocal fluorescence microscopy 5 min after staining: (a,b) K-(USY/Att.), (c,d) K-(USY/Bent.), (e,f) (USY/Bent.). Crosses indicate the cross-section's centers. The scale bars represent 100  $\mu\text{m}$ .

attapulgite provides oxygen basic sites, property desired for carrying out the aldol condensation reaction.<sup>[13]</sup>

Different from the attapulgite-based sample, the bentonite-containing body hardly showed any basicity. It should be noted that the existence of only a basic site is sufficient for  $\text{CO}_2$  to form monodentate carbonates, while both a basic site and a metal cation are required for bidentate carbonate formation.<sup>[10]</sup> Bentonite (Figure 4e) showed only a very weak signal for a monodentate carbonate species at  $\sim 1628\text{ cm}^{-1}$ , which was also seen for USY/Bent. (Figure 4g) and K-(USY/Bent.) (Figure 4f).

The concentration of basic sites determined from  $\text{CO}_2$ -TPD is shown in Table 1. The TPD data confirmed the lower number of basic sites in the K-(USY/Att.) technical catalyst compared to zeolite K-USY. The decrease in basicity after scaling-up is not just the result of zeolite dilution, given that attapulgite itself also showed a high amount of basic sites. It is most likely due to some clogging upon extrusion and subsequent incorporation of potassium. In particular, the basicity loss seen after K-grafting of the USY/Bent. material illustrates the weak interaction of  $\text{K}^+$  with the zeolite, which instead seems to interact more extensively with the clay. The very small amounts of  $\text{CO}_2$  desorbed from the bentonite-derived samples are in line with the limited basicity observed by  $\text{CO}_2$ -FT-IR spectroscopy.

Upon adsorption and desorption of pyridine as probe molecule, no FT-IR bands arising from the formation of pyridinium ion ( $\text{PyH}^+$ ) could be observed for the attapulgite-bound catalysts (Figure 5c–d), typically identified by the  $\sim 1545$  and the  $1640\text{ cm}^{-1}$  bands, associated with the presence of Brønsted acid sites.<sup>[47–48]</sup> In contrast, FT-IR bands ascribed to

hydrogen-bonded pyridine (H-bonded Py) – with absorption bands at  $\sim 1440\text{--}1450\text{ cm}^{-1}$  ( $\nu_{19b}$ ) and  $\sim 1580\text{--}1600\text{ cm}^{-1}$  ( $\nu_{8a}$ ) – and pyridine coordinated to Lewis acid sites (PyL), absorbing at  $\sim 1440\text{--}1460\text{ cm}^{-1}$  and  $\sim 1600\text{--}1635\text{ cm}^{-1}$ , were observed in every material. H-bonded pyridine was only seen at low evacuation temperatures, *i.e.* below  $150^\circ\text{C}$ , for the USY zeolite (Figure 5a) with the main bands at  $1446$  (see inset) and  $1596\text{ cm}^{-1}$ , illustrating its very weak acid character. After K-grafting (Figure 5b), the Lewis acid character of the sample increased, as indicated by the  $1590\text{ cm}^{-1}$  band, which is likely attributed to the formation of a PyL-complex formed on a  $\text{K}^+$  site. The PyL- $\text{K}^+$  band desorbed at  $200^\circ\text{C}$ , illustrating its weak strength. In the spectrum of the K-(USY/Att.) catalyst (Figure 5d), two clear PyL absorption bands could be observed: the first one at  $1591\text{ cm}^{-1}$ , created upon K-grafting, as previously observed for the K-USY catalyst (Figure 5b); and the second one at  $1608\text{ cm}^{-1}$ , arising from the occurrence of strong Lewis acid sites created upon attapulgite incorporation into the technical catalyst. For attapulgite (Figure 5c), three intense bands at  $\sim 1622$ ,  $1614$  and  $1609\text{ cm}^{-1}$  remained adsorbed till  $350^\circ\text{C}$ . These bands can be ascribed to PyL species formed on strong Lewis acid sites of the Attapulgite, associated with the presence of  $\text{Fe}^{3+}$ ,  $\text{Mg}^{2+}/\text{Ca}^{2+}$  and  $\text{Al}^{3+}$  cations (Table S2).<sup>[48–51]</sup>

For bentonite (Figure 5e), the absorption bands ascribed to pyridine interacting with both Brønsted ( $\text{PyH}^+$ ,  $1639$  and  $1545\text{ cm}^{-1}$ ) and Lewis (PyL,  $1621$  and  $1609\text{ cm}^{-1}$ ) acid sites were seen at  $150^\circ\text{C}$ . The bands at  $\sim 1621\text{ cm}^{-1}$  and  $\sim 1609\text{ cm}^{-1}$  are likely assigned to pyridine interacting with  $\text{Fe}^{3+}$  and  $\text{Al}^{3+}$  sites, respectively.<sup>[48,50]</sup> The  $\text{PyH}^+$ -band disappeared at  $250^\circ\text{C}$ , whereas

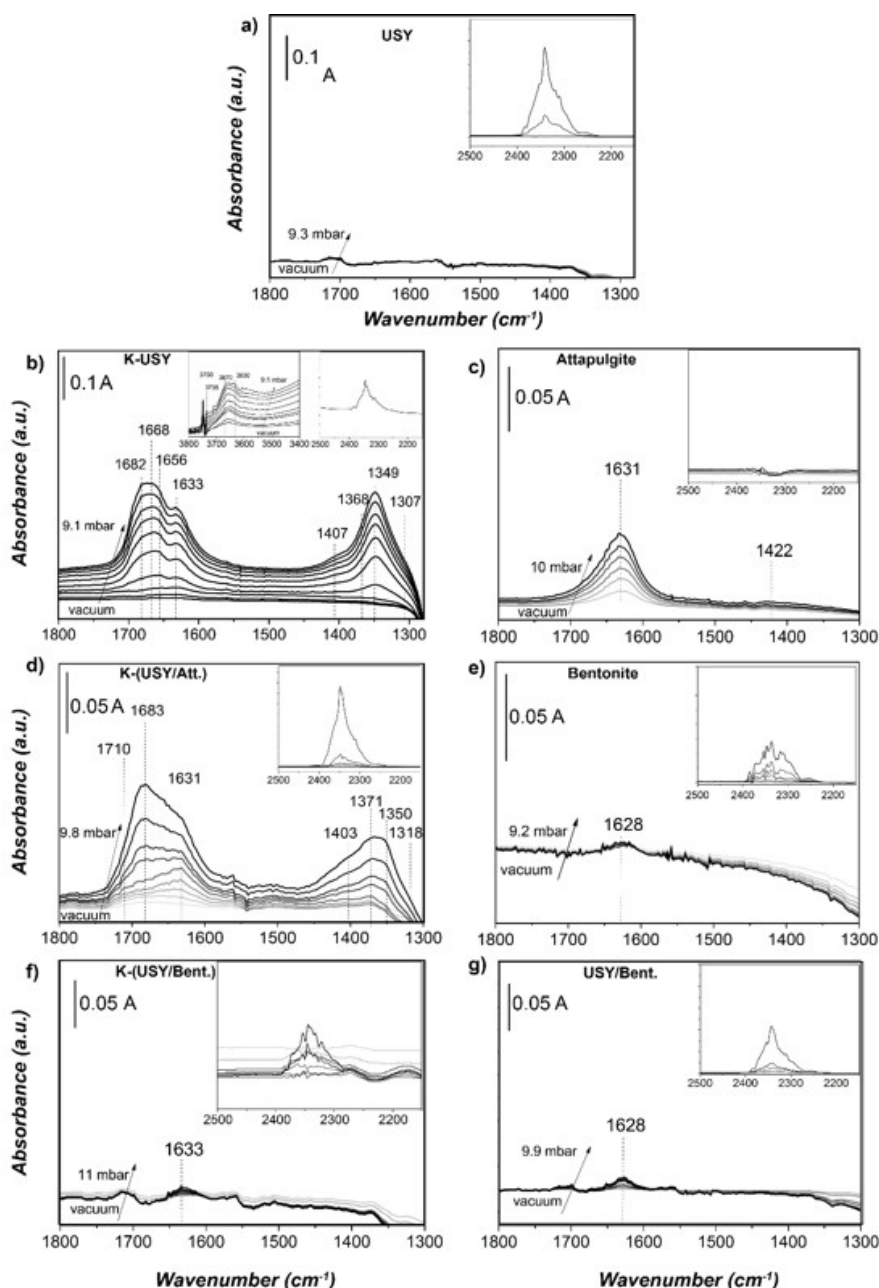


**Figure 4.** Normalized FT-IR spectra of the catalyst materials during CO<sub>2</sub> adsorption (from vacuum to P<sub>CO<sub>2</sub></sub> ~ 10 mbar) at room temperature: (a) zeolite USY, (b) zeolite K-USY, (c) attapulgite, (d) K-(USY/Att.), (e) bentonite, (f) K-(USY/Bent.) and (g) USY/Bent.

the PyL-bands remained adsorbed up to 300 °C, indicating the intermediate strength of the Brønsted acid sites and the strong nature of the Lewis acid sites, respectively. For USY/Bent. (Figure 5g) the same absorption bands as those observed for bentonite were seen at 150 °C, *i.e.* at ~1639, 1621 and 1609 cm<sup>-1</sup>. Besides, another absorption band at ~1596 cm<sup>-1</sup> – previously seen for zeolite USY at temperatures below 150 °C (Figure 5a) and assigned to H-bonded pyridine – was seen upon desorption at 200 °C, indicating the Brønsted acid character acquired upon bentonite incorporation. For the K-(USY/Bent.) catalyst (Figure 5f), the same absorption bands were seen as for non-grafted USY/Bent. However, the PyL band expected at

~1590 cm<sup>-1</sup> upon K-grafting procedure, in analogy with K-USY (Figure 5b) and K-(USY/Att.) (Figure 5d) catalysts, could not be seen, is in line with the low K loading achieved in the K-(USY/Bent.) catalyst. Besides, the absorption bands attributed to PyH<sup>+</sup>- and PyL-complexes present in USY/Bentonite catalyst (Figure 5g) seemed less intense after K-grafting (Figure 5f). Indeed, quantification of the acid sites at 150 °C confirmed that K-(USY/Bent.) had ~42% less acid sites than USY/Bent. (Table 1).

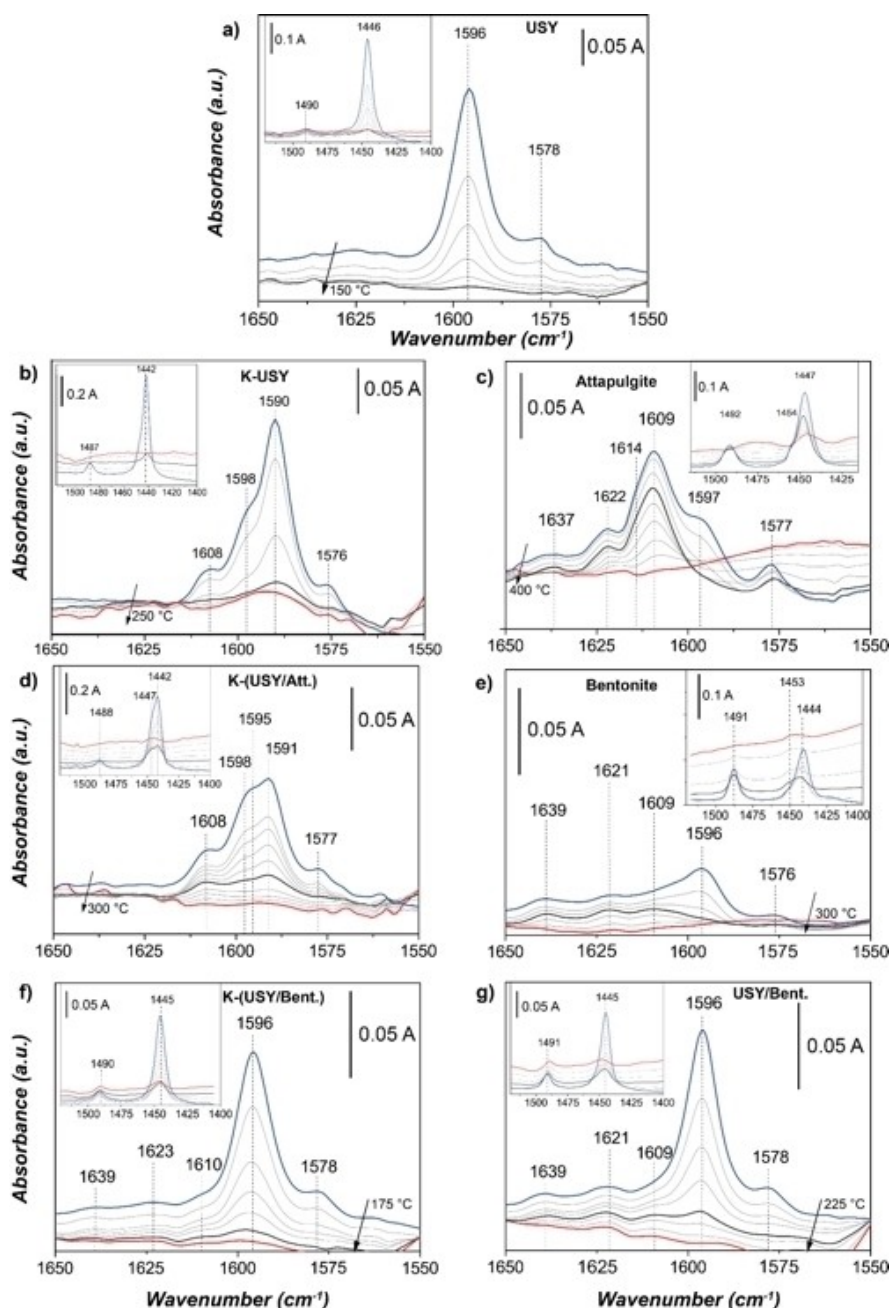


**Figure 5.** Normalized FT-IR spectra of the catalyst materials during pyridine desorption from room temperature (**blue**) till maximum desorption temperature (**red**): (a) USY, (b) K-USY, (c) Attapulgite, (d) K-(USY/Att.), (e) Bentonite, (f) K-(USY/Bent.) and (g) USY/Bent. Spectra highlighted in **grey** correspond to the spectra taken at 150 °C.

## 2.2. Catalytic Performance Evaluation

### 2.2.1. Catalyst activity and selectivity

*Operando* FT-IR (Figure S4 and Figure 6e,f) spectroscopic experiments with either on-line GC-FID (Figure 6a,b and Figure S5–S6) or on-line MS (Figure 6c,d and Figure S7) were performed to evaluate the catalytic performance in the vapor-phase aldol condensation of propanal, which were complemented with off-line GC-MS analysis. Following the same procedure than in a

former work<sup>[9]</sup> the reaction was followed for 1 h at atmospheric pressure and a reaction temperature of 400 °C, which is a typical temperature for the outlet of a pyrolytic stream.<sup>[52]</sup> The performance, on total mass weight-to-weight basis (Figure S5) and on zeolite weight-to-weight basis (Figure 6a) of (ground and pressed) shaped catalyst wafers were evaluated. Also the whole catalyst bodies were tested as such, to compare the effect of extrusion (i.e., on mass-transfer phenomena).

The on-line GC-FID results showed that the powdered catalyst K-USY was the most active, giving the highest propanal



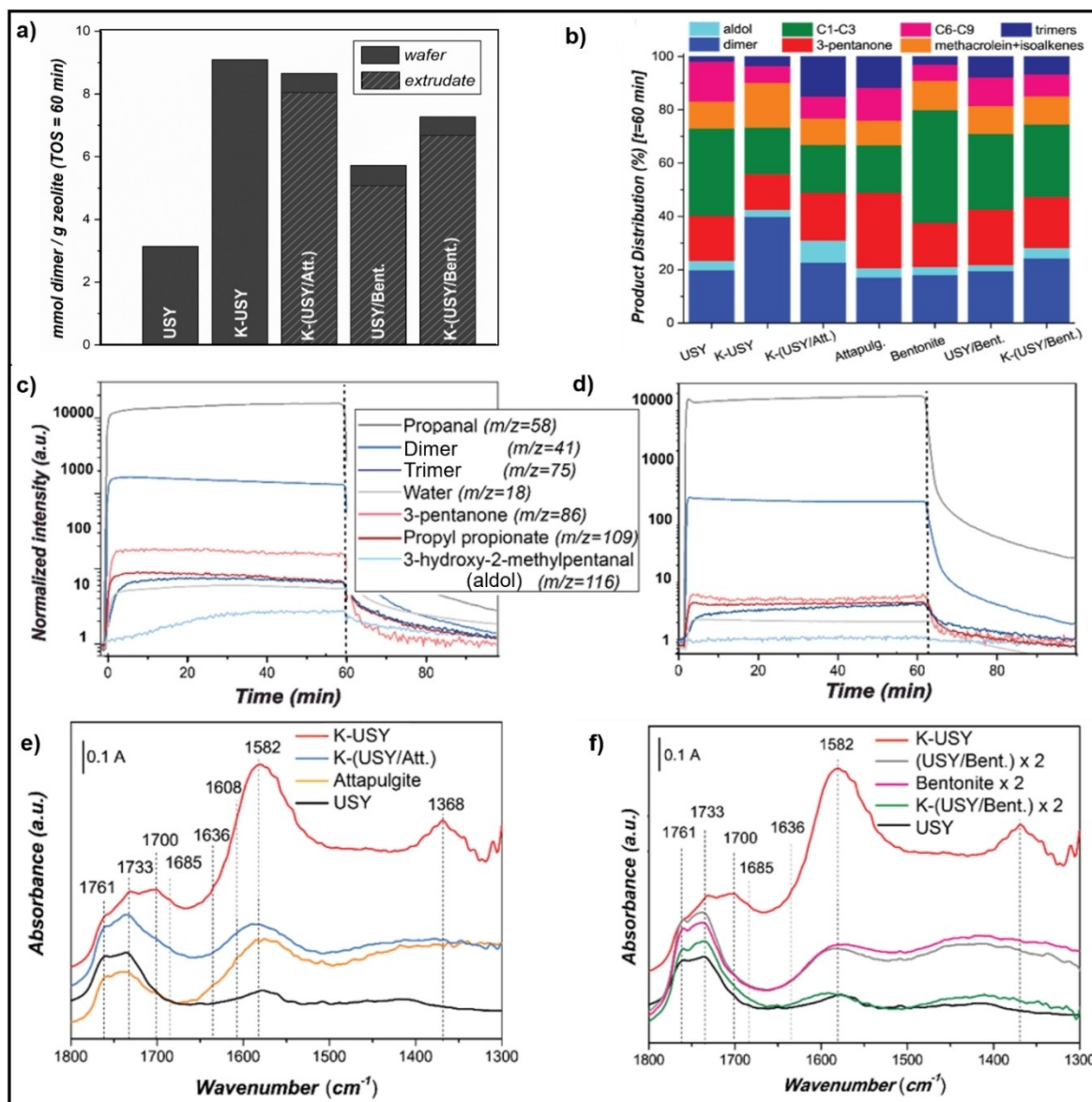


**Figure 6.** (a) mmol dimer formed for the zeolite-based materials of study (in wafer and in extrudate-patterned- shape), at  $t = 60$  min during vapor-phase propanal aldol condensation at 400 °C, as estimated from the on-line GC-FID. (b) Product distribution at  $t = 60$  min, as estimated from the on-line GC-FID and off-line GC-MS data for all wafer-shaped catalyst samples (see complementary Scheme S2 and Figure S5). (c–d) Selected on-line MS data obtained during 1 h for attapulgite (c) and K-(USY/Att.) (d) (see complementary Figure S7). (e–f) Selected FT-IR spectra for the attapulgite-bound (e) and bentonite-bound (f) catalyst series at 20 min of reaction (see complementary Figure S4). MS and IR results were normalized by total (zeolite and/or clay) mass weight.

conversion and yield towards the desired product, the aldol condensation dimer, i.e., 2-methyl-2-pentenal (Figure 6a, red series in Figure S5). For the sake of clarity, the main reaction routes derived from propanal reaction, with the main obtained products, are shown in Scheme S2. The low activity shown by the USY zeolite catalyst (black series in Figure S5) demonstrated the importance of introducing acid/base pairs by K-grafting. Zeolite K-USY proved highly selective, with only minor amounts of light C1–C3 by-products, such as acetaldehyde and ethanol<sup>[53–54]</sup> (Figure 6b) and by-products derived from the dimer such as methacrolein, 2-methylene-4-pentenal and other C6 iso-alkenes detected by GC-MS.<sup>[54]</sup> In contrast, low dimer yield was seen for the USY zeolite catalyst, for which 3-

pentanone and other additional oxygenated by-products, such as the Tishchenko propyl propionate product, and ketonization products were observed (Figure 6b).<sup>[9,55]</sup>

The technical K-(USY/Att.) catalyst showed a slightly lower dimer yield than the parent material, on zeolite weight-to-weight basis (Figure 6a). By-products identified included trimers (i.e., C9), such as 3-hydroxy-2-methylpentylpropionate, likely formed via either consecutive Tishchenko reactions<sup>[56]</sup> or via aldol condensation and subsequent Tishchenko reaction,<sup>[13]</sup> in addition to the dimers, propyl propionate and 3-pentanone (Figure 6b). A relatively high propanal conversion, but poor selectivity towards the dimers was shown for attapulgite, being more evident with increasing time-on-stream (Figure 6b, orange

series Figure S5). Instead, attapulgite was very selective towards 3-pentanone, with additional by-products, such as 3-hydroxycyclohexanone<sup>[57]</sup> being detected. Indeed, the MS results (Figure 6c) also suggested that attapulgite produced propyl propionate and 3-pentanone more extensively than K-(USY/Att.) (d) which, in turn showed a lower activity and selectivity than the K-USY catalyst (Figure S7b). The increasing m/z signal of the intermediate aldol product, 3-hydroxy-2-methylpentanal, seen for attapulgite suggests that dehydration might be the slowest stage in the surface reaction step.<sup>[9]</sup> In contrast, for the K-USY and K-(USY/Att.) catalysts, C–C coupling might be rate limiting in this Eley-Rideal type of reaction, given that the intermediate aldol product is not detected.<sup>[9]</sup>

K-(USY/Bent.) (green series in Figure S5) was less selective towards aldol condensation than K-(USY/Att.) catalyst (blue series), as K-(USY/Bent.) led mainly to 3-pentanone and other by-products (Figure 6b). Grafting of USY/Bent. with K again improved dimer selectivity (Figure 6a), though the non-grafted USY/Bent. catalyst showed mainly carboxylic acid and esters in addition to the dimer and 3-pentanone (b). The K-(USY/Bent.) catalyst also showed Tishchenko- and aldol condensed-derived linear oxygenated by-products. Bentonite only, with its high adsorption and swelling capacity,<sup>[58]</sup> gave an apparent high propanal conversion but low yields (magenta series in Figure S5), indicating that propanal just remained adsorbed in the catalyst, and pointing at mass-transfer limitations.

Mass-transfer was further revised when comparing the performance of the catalyst wafers and catalyst bodies samples for K-(USY/Att.), K-(USY/Bent.) and USY/Bent. (indicated by solid bars and area patterned, respectively, in Figure 6a, and Figure S6). Some differences were found, with apparent higher

conversion values for the USY/Bent. catalyst bodies (Figure S6), not associated to a higher activity but to longer retention of reactant/products, what evidences the existence of mass-transfer constrains which hinder diffusion. This observation is connected with the pore blockage observed upon characterization for bentonite-bound catalyst materials. By contrast, differences shown by the wafer and body shapes of the K-(USY/Att.) catalyst are not so significant, also in line with the better-preserved textural properties for the attapulgite-bound catalyst.

Figure 6e,f shows the comparative FT-IR spectra of the different catalysts at  $t=20$  min (see Figure S4 for evolution of operando spectra with increasing time-on-stream). In line with the catalytic data, K-(USY/Att.) (blue series, Figure 6e) showed lower selectivity towards the dimer than K-USY (red series) but higher than attapulgite (orange series). Lower aldol dimer and aldol trimer products were detected than with K-USY, as indicated by the lower intensity of the  $1700$  ( $\nu_{C=O}$ ) and  $1685$   $\text{cm}^{-1}$  ( $\nu_{C=C}$ ) stretching bands of the dimer, and  $1636$   $\text{cm}^{-1}$  ( $\nu_{C=C}$ ) band of the trimer (Table S2).<sup>[9]</sup> While product features can be clearly seen for K-USY, they were absent for the USY zeolite (black series) that exclusively show vapor-phase propanal. For both K-USY and K-(USY/Att.) catalysts, the infrared spectroscopic features of adsorbed propanal (as indicated by the negative intensity of the SiOH band at ca.  $3740$   $\text{cm}^{-1}$  in Figure S4a) dominate over those of the products, suggesting that the surface reaction is the limiting step of an Eley-Rideal type reaction, consistent with a previous proposal.<sup>[7,9]</sup> The FT-IR spectra of the bentonite-bound catalyst materials (Figure 7f) also confirm its poorer activity compared to the attapulgite-bound catalysts. Besides features of adsorbed propanal at  $2992$ – $2696$   $\text{cm}^{-1}$  (C–H stretch, Figure S4),  $1761$  and  $1733$   $\text{cm}^{-1}$

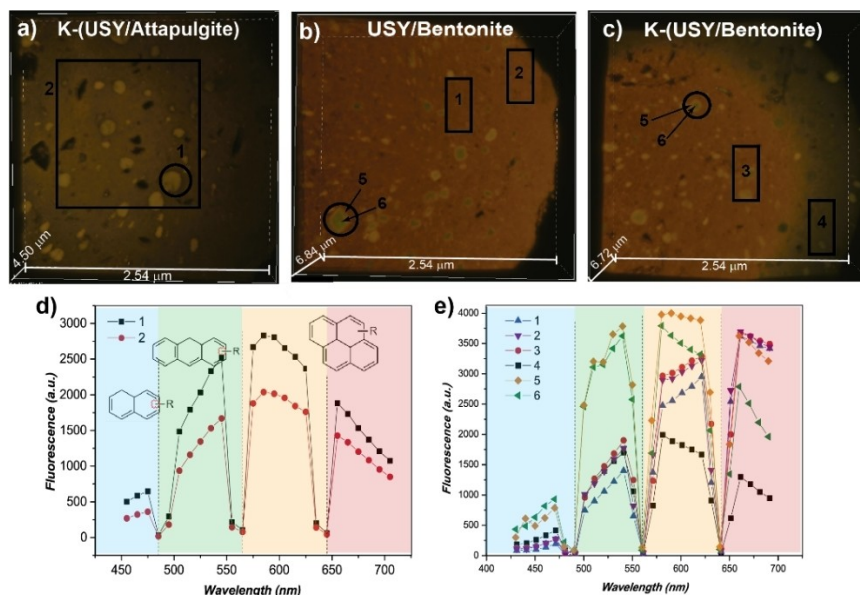


**Figure 7.** (a–c) Confocal fluorescence microscopy (CFM) images on the cross-section of spent K-(USY/Att.) (a), USY/Bent. (b) and K-(USY/Bent.) (c) catalyst bodies. (d–e) Corresponding spectral information of the regions of interest of K-(USY/Att.) (d), and USY/Bent. and K-(USY/Bent.) (e). Dashed vertical lines represent the excitation lasers, used simultaneously at  $\lambda_{\text{ex}}=404, 488, 561$  and  $642$  nm (background colors matching each) Background molecules are representative of the type of aromatic species expected according to their emission in each spectral region, and increasing in aromaticity with longer wavelengths.

(C=O stretch), only very weak aldol dimer features were detected at 1700 ( $\nu_{C=O}$ ) and 1685  $\text{cm}^{-1}$  ( $\nu_{C=C}$ ). No meaningful differences could be discerned by FT-IR spectroscopy among the bentonite-bound catalyst materials.

### 2.2.2. Catalyst stability

The formation of coke deposits, considered one of the main causes for catalyst deactivation in this reaction, was monitored during 1 h of reaction by FT-IR spectroscopy (Figure S4) and afterwards quantified by TGA-MS (Figure S8, Table 1). On TGA-MS curves it should be noted that the apparent differences in weight loss (dashed and continuous blue series) are not due to coke formation, but to the water content of the catalyst bodies, which are less efficiently pre-activated (to remove moisture and impurities) prior to reaction. The distribution of coke deposits over the extrudates was examined by CFM (Figure 7). FT-IR spectra showed the coke band at  $\sim 1582 \text{ cm}^{-1}$ <sup>[59]</sup> to be less intense for K-(USY/Att.) (Figure S4c) than for zeolite K-USY (Figure 7b), probably due to the lower C–C coupling activity. On the other hand, attapulgite (Figure 7d), very active but poorly selective, produced much more coke deposits. Expectedly, coke deposits were less pronounced for the bentonite-containing catalyst materials (Figure 7e–g), given their lower overall activity.

In line with the FT-IR spectroscopy observations, the amount of coke deposits formed on K-(USY/Att.) (blue series in Figure S8a, Table 1), with maximum combustion temperature at  $\sim 441^\circ\text{C}$ , was slightly lower than for the K-USY catalyst (red series). However, the nature of coke seemed softer on the latter, having a maximum combustion temperature at  $\sim 361^\circ\text{C}$ . The K-(USY/Att.) catalyst bodies showed exactly the same amounts and type of coke deposits than the catalyst wafer, evidencing the good diffusivity through the catalyst body, showing that the results from the catalyst wafer studies are relevant for the whole catalyst bodies. The coke deposits formed on the K-grafted (Figure S8b, green) and non-grafted USY/Bent. (grey) catalyst materials were very similar in their amount (both  $\sim 2$  wt.%, Table 1) and nature ( $T_{\text{max,comb.}} \sim 475$  and  $510^\circ\text{C}$  for the grafted- and non-grafted catalysts, respectively). Just as bentonite itself, the coke deposits in the USY/Bent. and K-(USY/Bent.) catalyst materials presented heterogeneities in poly-aromaticity, as evidenced by the shapes of the TGA curves from 450 to  $700^\circ\text{C}$ .

Chemical imaging of the spatial distribution of the coke deposits (and their conjugation) over the catalyst bodies was done by CFM to gain visual understanding of the role of each catalyst component in the overall chemical reaction. The CFM image of a cross-sectioned, spent K-(USY/Att.) extrudate (Figure 7a) showed areas of higher intensity (labelled as 1), whose emission spectra (Figure 7d) indicate that there is twice as much fluorescence than average (labelled as 2). Both areas showed similar profiles, though, with a  $\lambda_{\text{max}}$  at  $\sim 580 \text{ nm}$  indicative of the hard nature of the carbonaceous species (presumably related to the presence of 3 – or more- aromatic ring species).<sup>[60]</sup> The regions of high USY domains, as also

evidenced by the large amounts of coke fluorescence intensity correspond to rich-in-attapulgite domains, which apparently produce more and harder coke than the zeolite detected by TGA for attapulgite, likely as a result of its strong Lewis acid sites. While in K-(USY/Att.) the clay and zeolite seemed to be evenly distributed over the cross-section (Figure 7a), for the bentonite sample (Figure 7c) a shell could clearly be distinguished at the edge of the cross-section. This shell of fluorescence intensity is reminiscent of the bright shell seen after staining the fresh catalyst with FluoSpheres (see Figure 3c,e). This shell was shown to contain more potassium, and is here shown to contain less and softer coke (i.e. H-richer) (see 4 in Figure 7c,e) than the center of the cross section (see 3 in Figure 7c,e). Note that in the shell (see 4 in Figure 7c,e), the emission profile was very close to the one of the K-(USY/Att.) extrudate, with  $\lambda_{\text{max}} \sim 580 \text{ nm}$ . In line with the limited grafting, the nature of the coke formed in the middle of the cross-section of K-(USY/Bent.) was the same as the coke over USY/Bent. (see 1 and 2 in Figure 7b,e), being highly poly-aromatic with  $\lambda_{\text{max}} \sim 640 \text{ nm}$ . The above observations again suggest that K-grafting locally reduces coke deposit formation, as a result of Brønsted acid sites removal. Both catalyst bodies, namely USY/Bent. and K-(USY/Bent.), showed areas of yellowish fluorescence associated with bentonite domains, which upon detailed examination, show an outer yellow ring (5 in Figure 7c,e) and a greenish inside (6 in Figure 7c,e), where coke deposits might be of a softer nature (presumably related to the presence of naphthalenes).<sup>[61]</sup> These egg-shell clay domains were not observed for the attapulgite domains in the K-(USY/Att.) catalyst bodies, which looked more uniform in nature (see 1 in Figure 7a,d).

## 3. Conclusions

Two potassium grafted zeolite USY/clay (made with attapulgite or bentonite as binder material) extrudates were synthesized, extensively characterized and studied in the vapor-phase aldol condensation of propanal – as a model reaction for bio-oil upgrading via deoxygenation – with a combination of *operando* and in-situ characterization methods. A more intimate interaction was found between zeolite USY and attapulgite as compared to bentonite. Staining of attapulgite- and bentonite-bound catalyst bodies with a non-reactive fluorescent probe demonstrated that the accessibility of the catalyst body was impeded for the bentonite-based material, but not for the attapulgite-based material. Incorporation of the clay mineral also strongly modified the acid/basic properties of the final catalyst material. More specifically, it was found that extrusion with attapulgite led to the formation of strong Lewis acid sites, while the addition of bentonite created new weak Brønsted acid sites and strong Lewis acid sites, producing hardly any basicity, property desired for carrying out the aldol condensation reaction.

To preserve the crystallinity of the active USY zeolite component of the catalyst bodies, K-grafting had to be performed on the already synthesized materials rather than on

the powdered catalyst materials. It was found that less potassium was incorporated in the bentonite-based material, due to the impeded accessibility of the USY/bentonite combination. The catalyst body, with post alkali metal grafting resulted in a shell-like distribution of potassium. The necessity to expose the zeolite USY post-extrusion rather than pre-extrusion, does complicate catalyst synthesis as the binder present is not inert during the alkaline grafting procedure. Indeed, ion exchange can occur, for example between the Na<sup>+</sup> cations in bentonite and the K<sup>+</sup> in solution.

The two upscaling steps, i.e., clay addition and extrusion and post-grafting, led to a decrease in selectivity compared to the pure K-USY catalyst, in the case of the bentonite-bound material. These catalytic effects are in line with the lack of basicity and diffusivity hindrance observed upon characterization for the USY/Bent. catalysts. By contrast, the attapulgite-bound catalyst performed significantly better, showing a higher selectivity towards the aldol condensation products, associated to its superior textural properties and the presence of basic active sites. In terms of stability, while K-(USY/Att.) produced more coke than its bentonite-counterpart, the coke deposits were of softer nature (i.e. with higher H/C ratio), which may facilitate their removal and future catalyst regeneration. Therefore, attapulgite is clearly preferred over bentonite as binder material for synthesizing the zeolite USY-based catalyst bodies for bio-oil upgrading.

This study illustrates the complexity of the design of technical catalysts and the importance of in-depth understanding of the effects on properties and on catalytic performance for their scale-up. In upcoming academic studies more realistic scenarios of bio-oil deoxygenation may be explored to test the developed technical catalysts.

## Experimental Section

### Catalyst materials and their synthesis

An overview of the catalyst systems under study and their main characteristics are presented in Table S1. The technical extrudate catalysts were prepared by mixing USY zeolite (Tosoh Corporation, HSZ390HUA, Si/Al=405) with the relevant clay, attapulgite (Clay Minerals Society, PFI-1 palygorskite) or bentonite (Clay Minerals Society, SWy-3, Na-rich), in a 70 wt.% USY: 30 wt.% clay ratio using a Caleva Mixer Torque Rheometer 3. Prior to the addition of water, dry powders are mixed until an homogeneous mixture is formed. The drop-wise addition of water (~12 mL in total) leads to the formation of a thick paste, while the mixer torque rheometer constantly measures the level of humidity. Once the paste reached the optimum solid-to-liquid ratio, extrusion proceeded by using a Caleva Multi Lab equipped with extruder attachment (0.5 mm die plate). The formed cylinders were dried overnight, after which they were cut into 20 mm length extrudates. The extrudates were calcined in static air at 550 °C (5 °C/min) for 2 h. After extrusion, the catalysts were K-grafted by immersion into a 0.1 M solution of KOH in methanol for 30 min, according to literature protocol.<sup>[8]</sup> After washing with methanol, the solid catalysts were dried at 65 °C and calcined at 550 °C for 2 h. Inductively Coupled Plasma (ICP)-Optical Emission Spectrometry (OES) was used to determine the composition of attapulgite and bentonite, as shown in Table S2. Note that

trace elements present in less than 0.5 wt% in both clays are not listed. The elements detected include Ba, Cr, Ga, Mn, Ti and V for attapulgite; Mn, S, Sr, Ti, V and Zr for bentonite.

### Inductively coupled plasma – optical emission spectrometry

Inductively Coupled Plasma - Optical Emission Spectrometry (ICP-OES) measurements were performed on a Spectro Arcos ICP-OES equipped with a Paschen-Runge spectrometer. Emission corresponding to K, Mg and Al was measured. Prior to analysis the catalyst samples were dissolved using HF and diluted with a 1 M HNO<sub>3</sub> solution.

### Scanning electron microscopy – energy-dispersive x-ray spectroscopy

Scanning Electron Microscopy (SEM) was performed on a FEI Helios nanolab 600 DualBeam microscope. The electron beam operated at 2.00 kV at a current of 0.20 nA. The images were obtained from the secondary electrons with a dwell time of 1 μs. Energy-Dispersive X-ray spectroscopy (EDX) mapping was performed using an Oxford instruments silicon drift detector X-Max energy dispersive spectroscopy with an electron beam at 15.00 kV and a current of 0.80 nA. Prior to the SEM measurements, the samples were prepared by placing the cross-sectioned extrudates on a sample holder, coated with Pt in a Cressington 208\_HR sputter coater using a Pt target. Sputtering was operated at 0.08 mbar Ar atmosphere with an applied current of 40 mA. The samples were rotated at a slight tilt to obtain a homogeneous layer of Pt. The coating was done for 200 s resulting in a layer of ca. 10 nm.

### X-ray diffraction

X-Ray Diffraction (XRD) patterns were obtained at room temperature from 5 to 90 2θ° with a Bruker-AXS D2 Phaser powder X-ray diffractometer using a cobalt Kα<sub>1,2</sub> (λ<sub>1,2</sub>=1.79026 Å) source, operated at 30 kV. A step size of 0.05 (2θ)° and a scan speed of 1.0 s were applied.

### Argon and nitrogen physisorption

Textural properties of the materials were studied by Ar physisorption at -196 °C using a Micromeritics Tristar 3000 equipment. The Brunauer-Emmett-Teller (BET) method was applied to calculate the surface area. The t-plot method was applied to obtain the micropore volume and external surface area. The Barret-Joyner-Halenda (BJH) model was used on the desorption branch to determine the mesopore volume.

### Fourier-transform – infrared spectroscopy

For the adsorption and desorption of probe molecules, such as CO<sub>2</sub> and pyridine followed by Fourier Transform Infrared (FT-IR) spectroscopy ~15 mg of the extrudates were ground and pressed into self-supporting wafers (ø=12 mm). The obtained sample was placed into the measurement cell. For the measurements 16 scans per spectrum were performed on a Perkin Elmer System 2000 with a DTGS detector. The spectra were recorded in transmission mode in the spectral range of 4000–400 cm<sup>-1</sup>, with a resolution of 4 cm<sup>-1</sup>. The catalyst was first dried in the cell under vacuum (~10<sup>-5</sup> mbar) using a temperature ramp of 5 °C/min to a final temperature of 550 °C. This temperature was then kept constant for 1 h, after which the sample was cooled down to room temperature. For pyridine (Sigma-Aldrich, 99%) measurements (Pyridine-FT-IR), once the

sample was cooled down, pyridine vapors ( $P_{py}$ , ~11 mbar) were allowed into the cell and onto the catalyst. After saturation for 30 min, the cell was set under vacuum (~ $10^{-5}$  mbar) for 5 min to remove physisorbed pyridine from the sample. Subsequently, desorption was carried from room temperature to 550 °C, at a heating ramp of 5 °C/min. During the temperature program desorption (TPD), FT-IR spectra were subsequently taken every 25 °C to study the thermal pyridine desorption. For CO<sub>2</sub> adsorption and subsequent desorption (CO<sub>2</sub>-FT-IR spectroscopy), doses of CO<sub>2</sub> (Linde, 99.99%) were allowed onto the sample till a maximum pressure of ~10 mbar at room temperature. The interaction of CO<sub>2</sub> with the catalyst was monitored by recording FT-IR spectra between the doses of CO<sub>2</sub> at room temperature. Subsequently, the desorption was also gradually monitored until vacuum was reached.

### Temperature programmed desorption

Temperature Programmed Desorption (TPD) measurements of CO<sub>2</sub> were performed on a Micromeritics ASAP2920 apparatus. Approximately 100 mg of sample were dried *in-situ* by flowing He (50 mL/min), while a temperature ramp of 10 °C/min up to 550 °C was applied. After this temperature was held for 2 h, the sample was then cooled down to 50 °C. Afterwards, CO<sub>2</sub> was flown through the catalyst bed, by pulsing 10% CO<sub>2</sub>/He (Linde) until saturation. Desorption was started by flushing with He flow (50 mL/min) for 1 h and subsequently heating the sample up to 550 °C (10 °C/min) to induce CO<sub>2</sub> desorption. For the calculation of the number of basic sites, it was assumed that only one molecule of CO<sub>2</sub> can adsorb on a single site.

### Confocal fluorescence microscopy

Confocal Fluorescence Microscopy (CFM) experiments were performed on a Nikon Eclipse 90i confocal microscope with a 100× 0.73 NA dry objective in reflectance mode. These experiments were performed on the catalyst bodies. During the measurements, a catalyst body was placed in an open *in-situ* cell (Linkam Instruments, FTIR 600) equipped with a temperature controller (Linkam TMS 93). The microscope was equipped with a Nikon A1 scan head. Coke deposits present in the spent catalyst bodies were visualized by CFM at room temperature with no further preparation except for cross-sectioning the particle in the middle. The accessibility of the catalyst bodies (i.e., K-(USY/Att.), K-(USY/Bent.) and USY/Bent.) was assessed by staining the material with carboxylate-modified microspheres of 0.02 μm size, FluoSpheres (ThermoFischer, 2% solids), of green-like/yellow fluorescence. Details of this method can be found in a recent publication of our group.<sup>[40]</sup> Staining (~15 μL for saturation) was done on the external surface of the catalyst bodies, and the analysis was performed at the center of the cross-section.

### Thermogravimetric-mass spectrometry analysis

Thermogravimetric Analysis (TGA) was performed with a Perkin Elmer Pyris 1 TGA thermogravimetric analyzer coupled to a Pfeiffer Vacuum Omnistar mass spectrometer (MS). Approximately 10 mg of spent catalyst was used for this analysis. An air flow (60 mL/min) was employed during thermal treatment, which consisted of heating the sample from 50 °C up to 800 °C with a ramp of 10 °C/min. The MS detector was set to monitor the evolution of O<sub>2</sub>, H<sub>2</sub>O, CO, C and CO<sub>2</sub>.

### Testing

Catalyst samples were prepared by grinding the catalyst and pressing it into self-supporting wafers (~15 mg,  $\phi$  = 12 mm) by applying a pressure of 90–260 MN/m<sup>2</sup> for 20 s. The obtained sample was placed in a reaction cell. Before reaction, the sample was activated under O<sub>2</sub>-flow (10 mL/min, Linde, 99.999%) at 150 °C (10 °C/min) for 30 min and subsequently at 400 °C (10 °C/min) for additional 30 min. Following the activation, the flow was switched to the carrier gas N<sub>2</sub> (10 mL/min) for 30 min. The reaction was started by flowing part of the N<sub>2</sub> gas flow (5 mL/min) through a propanal-containing saturator kept at constant temperature of 0 °C. A second stream in parallel of N<sub>2</sub> gas (5 mL/min) was flushed for dilution of the reactant stream. After 1 h of reaction, the propanal flow was stopped.

In an operando set-up combining simultaneous Fourier-Transform Infrared (FT-IR) spectroscopy with on-line Mass Spectroscopy (MS) or on-line Gas Chromatography with Flame Ionization Detector (GC-FID), the vapor-phase aldol condensation of propanal was monitored over the wafers of the different catalysts under study. The experimental set-up is schematically illustrated in Scheme S1a. FT-IR spectra were recorded on a Bruker Tensor 27 equipped with an internal DLaTGS detector. The spectra with a resolution of 4 cm<sup>-1</sup> were obtained by collecting 32 scans over a region from 4000 cm<sup>-1</sup> to 400 cm<sup>-1</sup>. On-line MS data was obtained with an Omnistar Pfeiffer Vacuum mass spectrometer with quadrupole detector. The data were recorded using Quadstar 32-Bit. Note that the MS measurements do not allow for quantitative analysis, given that the response is not linear and differs greatly from ion to ion. Every MS signal was normalized by the catalyst weight, by the m/z signal of the carrier gas, N<sub>2</sub> = 28, and by the initial signal prior to reaction (directly by-passed to the MS).

Complementary on-line GC-FID measurements were performed for quantitative analysis of catalytic performance. GC experiments were performed on a CompactGC4.0 Chromatograph (Interscience) with three gas analyzer channels: one with TCD detector for measuring permanent gases, e.g. O<sub>2</sub>, N<sub>2</sub>, Ar; and two with FID detectors, for light hydrocarbons (C1–C3) and heavier hydrocarbons (C4–C8), respectively. The latter is the main FID channel used, with the detector set at 150 °C and with a MXT-5 column (15 m, 0.28 mm, 1 μm). The temperature of the column was kept constant at 55 °C, while the injections (1 μL) were performed at 80 °C and 125 kPa. From the chromatograms obtained during reaction, conversion was calculated as  $X = 1 - n_{out,prop}/n_{in,prop}$ , where  $n_{out,prop}$  is the moles of propanal leaving the reaction cell and  $n_{in,prop}$  is the moles of propanal inserted in the reaction cell, at a given time. The product yields were calculated as  $Y_i = n_i/(n_{in,prop} \cdot \nu_i)$ , where  $n_i$  is the moles of the product and  $\nu_i$  the stoichiometric ratio between the product and propanal. The main products (dimer, aldol product and 3-pentanone) yields were calculated based on calibration curves, referencing to N<sub>2</sub> as internal standard (quantified by the TCD detector channel). The rest of the products were identified with auxiliary GC-MS measurements (vide infra) and grouped in families for a rough product distribution estimation.

For the *in-situ* FT-IR spectroscopy measurements combined with off-line GC-MS the experimental set-up used is shown in Scheme S1b. Note that the only difference with the operando set-up in Scheme S1a is that the line to the MS/GC-FID was replaced by a cold trap at -196 °C where the reaction products were condensed for ex-situ GC-MS analyses.

For both the *in-situ* and the operando measurements identical procedures for sample preparation, activation, reaction and desorption were used. The products condensed during 1 h of

reaction were collected with 0.6 mL 1,4-dioxane as solvent and placed in a GC sampling vial for analysis.

GC-MS experiments were performed on a GCMS-QP2010 Shimadzu apparatus with a VF-5MS column (30 m, 0.25 mm, 0.25 μm) equipped with an AOC-20i auto-injector. Each injection (1 μL) was performed at 265 °C with column flow of 2.0 mL/min.

Analogous to the runs on wafer-shaped catalyst samples, the original extrudate-shaped K-(USY/Attapulgate), USY/Bentonite and K-(USY/Bent.) catalysts were also reacted in the same reaction cell used for the catalyst wafers. Pre-treatment and reaction conditions for the catalyst bodies were exactly the same as for the catalyst wafers. The reactions were followed by on-line MS, on-line GC-FID and by off-line GC-MS, the latter by means of a cold trap.

## Acknowledgements

This work was funded by the European Union Seventh Framework Programme (FP7/2007–2013) under Grant Agreement No. 604307 (CASCATBEL project). M. Versluijs-Helder (Utrecht University, UU) is acknowledged for performing the TGA measurements and H.C. de Waard (UU) is acknowledged for performing the ICP-OES analyses. J. Wijten (UU) is thanked for taking the SEM-EDX pictures.

## Conflict of Interest

The authors declare no conflict of interest.

**Keywords:** Bio-oil upgrading · catalyst scale-up · clay binders · extrudates · aldol condensation · operando spectroscopy

- P. M. Mortensen, J. D. Grunwaldt, P. A. Jensen, K. G. Knudsen, A. D. Jensen, *Appl. Catal. A* **2011**, *407*, 1–19.
- CASCATBEL project, [www.cascatel.eu](http://www.cascatel.eu) (last accessed on 15.06.2020).
- R. W. Snell, E. Combs, B. H. Shanks, *Top. Catal.* **2010**, *53*, 1248–1253.
- M. J. Climent, A. Corma, V. Fornés, R. Guil-López, S. Iborra, *Adv. Synth. Catal.* **2002**, *344*, 1090–1096.
- H. Hattori, *Mater. Chem. Phys.* **1988**, *18*, 533–552.
- E. G. Rodrigues, T. C. Keller, S. Mitchell, J. Pérez-Ramírez, *Green Chem.* **2014**, *16*, 4870–4874.
- B. Puértolas, T. C. Keller, S. Mitchell, J. Pérez-Ramírez, *Appl. Catal. B* **2016**, *184*, 77–86.
- T. C. Keller, K. Desai, S. Mitchell, J. Pérez-Ramírez, *ACS Catal.* **2015**, *5*, 5388–5396.
- A. M. Hernández-Giménez, J. Ruiz-Martínez, B. Puértolas, J. Pérez-Ramírez, P. C. A. Bruijninx, B. M. Weckhuysen, *Top. Catal.* **2017**, *60*, 1522–1536.
- J.-L. Kao, K. R. Clem, T. H. Vanderspurt, S. C. Fung (ExxonMobil), US-6506703B1, **1998**.
- A. Zúkal, V. Patzelová, U. Lohse, *Zeolites* **1986**, *6*, 133–136.
- T. C. Keller, M. Položij, B. Puértolas, H. V. Thang, P. Nachtigall, J. Pérez-Ramírez, *J. Phys. Chem. C* **2016**, *120*, 4954–4960.
- H. Hattori, *Chem. Rev.* **1995**, *95*, 537–558.
- H. Hernando, B. Puértolas, P. Pizarro, J. Feroso, J. Pérez-Ramírez, D. P. Serrano, *ACS Sustainable Chem. Eng.* **2019**, *7*, 18027–18037.
- P. G. Menon, *Chem. Rev.* **1994**, *94*, 1021–1046.
- S. Mitchell, N.-L. Michels, J. Pérez-Ramírez, *Chem. Soc. Rev.* **2013**, *42*, 6094–6112.
- G. T. Whiting, F. Meirer, M. M. Mertens, A.-J. Bons, B. M. Weiss, P. A. Stevens, E. de Smit, B. M. Weckhuysen, *ChemCatChem* **2015**, *7*, 1312–1321.
- B. Kraushaar-Czarnetzki, S. P. Müller, in: *Synthesis of Solid Catalysts*, (Eds.: K. P. de Jong), Wiley-VCH, Weinheim, **2009**, pp. 173–199.
- S. Mitchell, N.-L. Michels, K. Kunze, J. Pérez-Ramírez, *Nat. Chem.* **2012**, *4*, 825–831.
- G. T. Whiting, A. D. Chowdhury, R. Oord, P. Paalanen, B. M. Weckhuysen, *Faraday Discuss.* **2016**, *188*, 369–386.
- J. S. J. Hargreaves, A. L. Munnoch, *Catal. Sci. Technol.* **2013**, *3*, 1165–1171.
- R. V. Jasra, B. Tyagi, Y. M. Badheka, V. N. Choudary, T. S. G. Bhat, *Ind. Eng. Chem. Res.* **2003**, *42*, 3263–3272.
- E. T. C. Vogt, G. T. Whiting, A. Dutta Chowdhury, B. M. Weckhuysen, *Adv. Catal.* **2015**, *58*, 143–314.
- S. P. Verkleij, G. T. Whiting, D. Pieper, S. Parres-Esclapez, S. Li, M. M. Mertens, M. Janssen, A. J. Bons, M. Burgers, B. M. Weckhuysen, *ChemCatChem* **2019**, *11*, 4788–4796.
- S. P. Verkleij, G. T. Whiting, S. Parres-Esclapez, S. Li, M. M. Mertens, M. Janssen, A. J. Bons, M. Burgers, B. M. Weckhuysen, *ChemCatChem* **2020**, *12*, 5465–5475.
- S. P. Verkleij, G. T. Whiting, S. Parres-Esclapez, S. Li, M. M. Mertens, A. J. Bons, M. Burgers, B. M. Weckhuysen, *Catal. Sci. Technol.*, **2018**, *8*, 2175–2185.
- M. A. Uguina, J. L. Sotelo, D. P. Serrano, *Appl. Catal.*, **1991**, *76*, 183–198.
- A. de Lucas, J. L. Valverde, P. Sánchez, F. Dorado, M. J. Ramos, *Ind. Eng. Chem. Res.* **2004**, *43*, 8217–8225.
- A. de Lucas, J. L. Valverde, P. Sánchez, F. Dorado, M. J. Ramos, *Appl. Catal. A* **2005**, *282*, 15–24.
- P. Sánchez, F. Dorado, A. Fúnez, V. Jiménez, M. J. Ramos, J. L. Valverde, *J. Mol. Catal. A* **2007**, *273*, 109–113.
- N. L. Michels, S. Mitchell, J. Pérez-Ramírez, *ACS Catal.* **2014**, *4*, 2409–2417.
- Z. Vajglova, N. Kumar, P. Mäki-Arvela, K. Eranen, M. Peurla, L. Hupa, M. Nurmí, M. Toivakka, D. Y. Murzui, *Ind. Eng. Chem. Res.* **2019**, *58*, 18084–18096.
- J. Zecevic, G. Vanbutsele, K. P. de Jong, J. A. Martens, *Nature* **2015**, *528*, 245–248.
- Z. Vajglova, N. Kumar, M. Peurla, L. Hupa, D. A. Sladkovskiy, D. Y. Murzui, *Ind. Eng. Chem. Res.* **2019**, *58*, 10875–10885.
- IZA Database, FAU (last accessed on 30.03.2018). [europe.iza-structure.org/IZA-SC/framework.php?STC=FAU](http://europe.iza-structure.org/IZA-SC/framework.php?STC=FAU).
- K. S. W. Sing, D. H. Everett, R. A. W. Haul, L. Moscou, R. A. Pierotti, J. Rouquerol, *Pure Appl. Chem.* **1985**, *57*, 603–619.
- K. S. W. Sing, R. T. Williams, *Adsorpt. Sci. Technol.* **2004**, *22*, 773–782.
- W. F. Bradley, *Mineralogist* **1940**, *25*, 405–410.
- G. Wei, Y. Li, L. Zhang, S. Cai, T. Zhu, Z. Li, J. Mo, *Appl. Clay Sci.* **2018**, *152*, 342–351.
- G. T. Whiting, N. Nikolopoulos, I. Nikolopoulos, A. D. Chowdhury, B. M. Weckhuysen, *Nat. Chem.* **2019**, *11*, 23–31.
- L. C. Lavalley, *Catal. Today* **1996**, *27*, 353–376.
- S. Bordiga, C. Lamberti, F. Bonino, A. Travert, F. Thibault-Starzyk, *Chem. Soc. Rev.* **2015**, *44*, 7262–7341.
- C. R. Ho, S. Shylesh, A. T. Bell, *ACS Catal.* **2016**, *6*, 939–948.
- E.-M. Köck, M. Kogler, T. Bielz, B. Klötzer, S. Penner, *J. Phys. Chem. C* **2013**, *117*, 17666–17673.
- A. Vimont, F. Thibault-Starzyk, J. C. Lavalley, *J. Phys. Chem. B* **2000**, *104*, 286–291.
- T. K. Phung, L. Proietti Hernández, A. Lagazzo, G. Busca, *Appl. Catal. A* **2015**, *493*, 77–89.
- X. Liu, in: *Zeolite characterization and catalysis: A tutorial*, (Eds.: A. W. Chester, E. G. Derouane), Springer, Berlin, **2010**, pp. 197–222.
- T. K. Phung, M. M. Carnasciali, E. Finocchio, G. Busca, *Appl. Catal. A* **2014**, *470*, 72–80.
- I. M. Hill, S. Hanspal, Z. D. Young, R. J. Davis, *J. Phys. Chem. C* **2015**, *119*, 9186–9197.
- S. H. Begum, C. T. Hung, Y. T. Chen, S. J. Huang, P. H. Wu, X. Han, S. B. Liu, *J. Mol. Catal. A* **2016**, *423*, 423–432.
- J. Feroso, H. Hernando, P. Jana, I. Moreno, J. Prech, C. Ochoa-Hernández, P. Pizarro, J. M. Coronado, J. Cejka, D. P. Serrano, *Catal. Today* **2016**, *277*, 171–181.
- A. V. Bridgwater, *Biomass Bioenergy* **2012**, *38*, 68–94.
- A. Gangadharan, M. Shen, T. Sooknoi, D. E. Resasco, R. G. Mallinson, *Appl. Catal. A* **2010**, *385*, 80–91.
- T. Q. Hoang, X. Zhu, T. Sooknoi, D. E. Resasco, R. G. Mallinson, *J. Catal.* **2010**, *271*, 201–208.
- T. C. Keller, S. Isabettini, D. Verboekend, E. G. Rodrigues, J. Pérez-Ramírez, *Chem. Sci.* **2014**, *5*, 677–684.

- [56] A. Miyano, D. Tashiro, Y. Kawasaki, S. Sakaguchi, Y. Ishii, *Tetrahedron Lett.* **1998**, *39*, 6901–6902.
- [57] K. Ebitani, K. Motokura, K. Mori, T. Mizugaki, K. Kaneda, *Org. Chem.* **2006**, *71*, 5440–5447.
- [58] A. G. Clem, R. W. Doehler, *Clays Clay Miner.* **1961**, *10*, 272–283.
- [59] H. G. Karge, W. Nießen, H. Bludau, *Appl. Catal. A* **1996**, *146*, 339–349.
- [60] Q. Qian, J. Ruiz-Martinez, M. Mokhtar, A. M. Asiri, S. A. Al-Thabaiti, S. N. Basahel, H. E. van der Bij, J. Kornatowski, B. M. Weckhuysen, *Chem. Eur. J.* **2013**, *19*, 11204–11215.
- [61] G. T. Whiting, N. Nikolopoulos, I. Nikolopoulos, A. D. Chowdhury, B. M. Weckhuysen, *Nat. Chem.* **2019**, *11*, 23–31.

---

Manuscript received: November 15, 2020  
Revised manuscript received: January 9, 2021  
Accepted manuscript online: January 15, 2021  
Version of record online: February 16, 2021